Electronic Supplementary Material (ESI) for Inorganic Chemistry Frontiers.

Supporting Information

Strong anisotropic second-order nonlinear optical response in 0D lead-free chiral perovskite single-crystalline microwire arrays

Meiqiu Dong,[a] Binshuai Wang,[f] Ziwei Yu,[a] Jinjin Zhao,[d,e] Xinyi Li,[a] Yue Fu,[a] Yangwu Guo,*[a] Yingjie Zhao,*[c] Hanfei Gao,*[a] Lei Jiang[a,b] and Yuchen Wu[a,b]

[a]Ji Hua Laboratory, Foshan, Guangdong, 528000, P.R. China

Emails: guoyangwu15@mails.ucas.ac.cn; gaohanfei15@mails.ucas.ac.cn

[b]CAS Key Laboratory of Bio-inspired Materials and Interfacial Science, Technical Institute of Physics and Chemistry, Chinese Academy of Sciences, Beijing, 100190, P.R. China

[c]College of Chemistry, Zhengzhou University, Zhengzhou 450001, P.R. China

Email: zhaoyingjie5@zzu.edu.cn

[d]Department of Physics, Shanxi Datong University, Datong, 037009, P.R. China

[e]Shanxi Province Key Laboratory of Microstructure Functional Materials Institute of Solid State Physics, Shanxi Datong University, Datong, 037009, P.R. China

[f]Department of Urology, Peking University Third Hospital, Beijing, 100191, P.R. China

Keywords: chiral, 0D perovskite, microwire arrays, single crystal, second harmonic generation

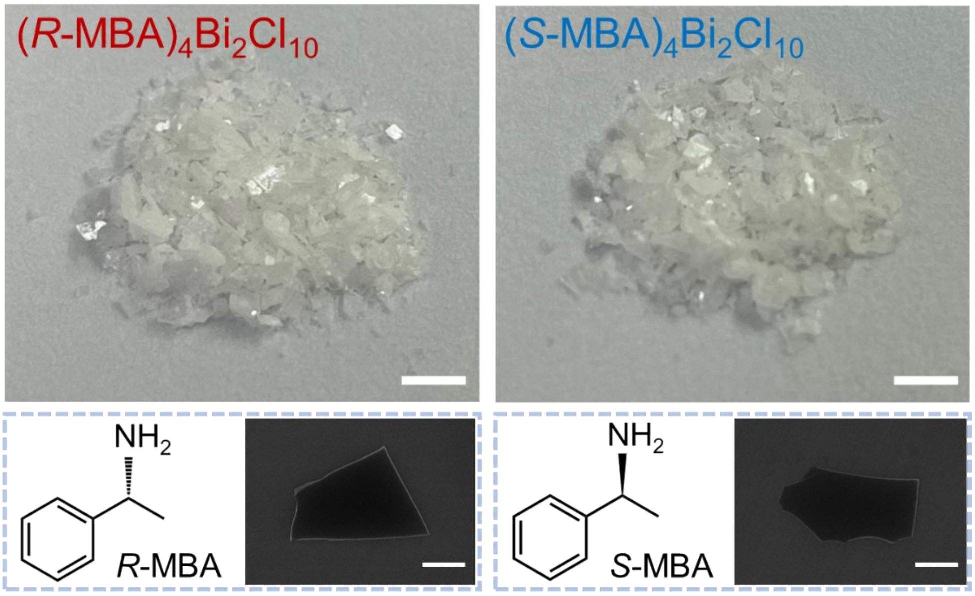

Fig. S1 Optical photographs of the as-synthesized colorless plate crystals and SEM images of the exfoliated crystal of 0D (R/S-MBA)$_4$Bi$_2$Cl$_{10}$ chiral perovskites. Scale bars: top, 3 mm; bottom, 1 μm.

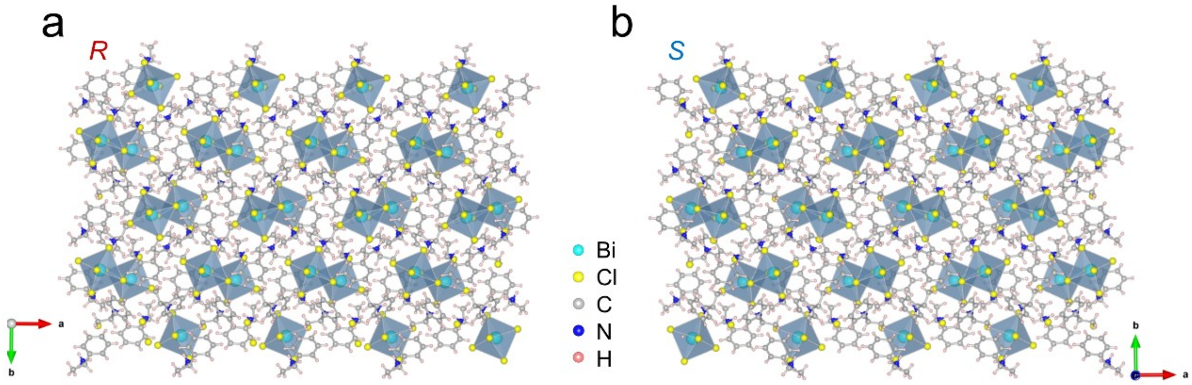

Fig. S2 The overall view of crystal structures of (a) (R-MBA)$_4$Bi$_2$Cl$_{10}$ and (b) (S-MBA)$_4$Bi$_2$Cl$_{10}$.

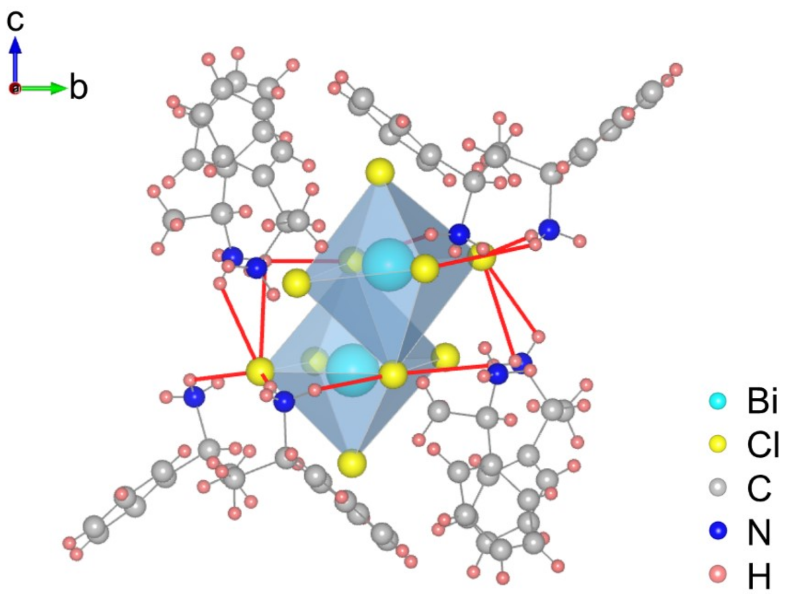

Fig. S3 The hydrogen bonds (red lines) around $[Bi_2Cl_{10}]^{4-}$ building block.

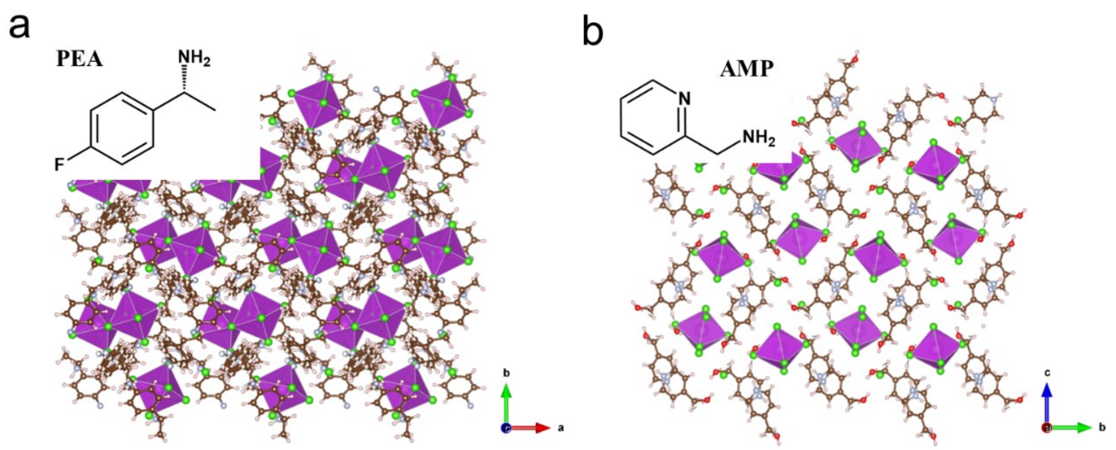

Fig. S4 Schematic structures of 0D perovskite crystals (a) $PEA_4Bi_2Cl_{10}$ and (b) $AMP_2BiCl_7 \cdot H_2O$. Insets are the corresponding ammonium molecules.

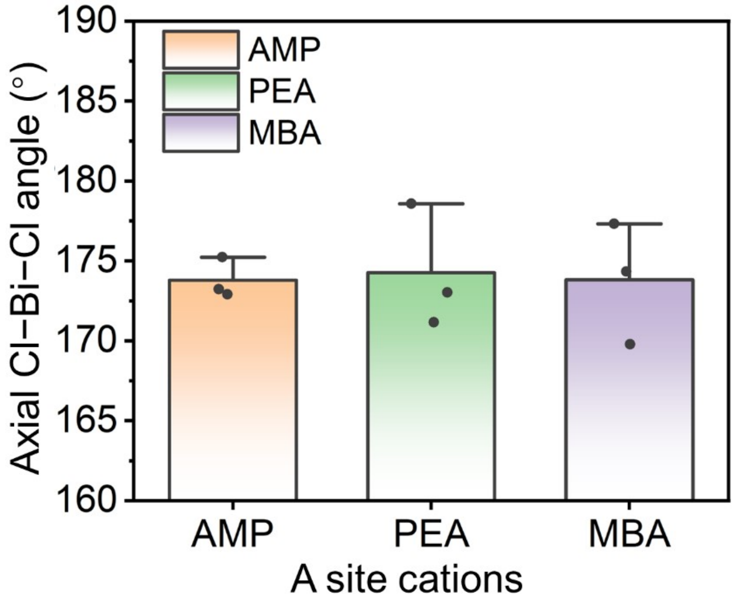

Fig. S5 The distribution of axial Cl−Bi−Cl angles in crystal structures of perovskites with different A-site cations.

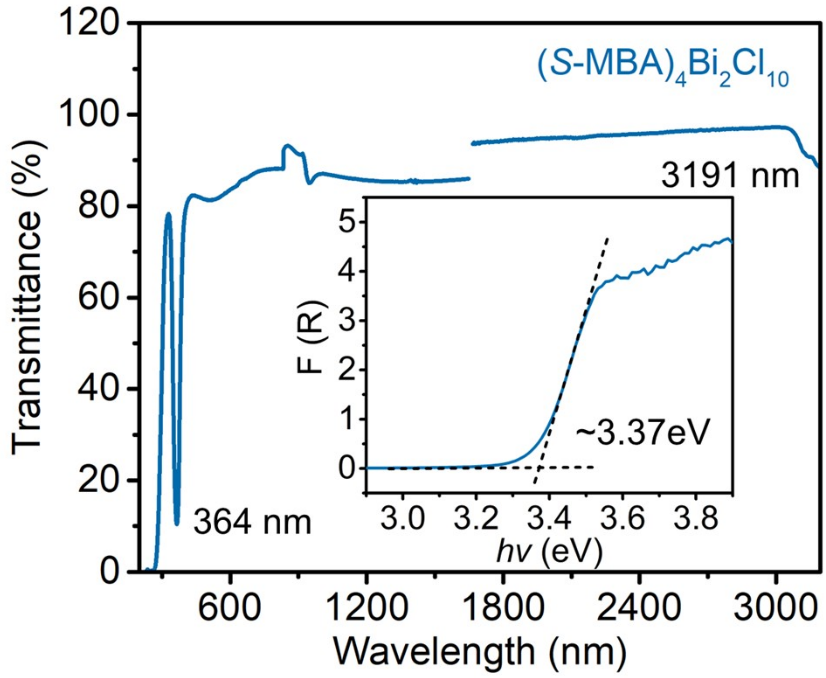

Fig. S6 UV-vis-NIR transmittance spectrum and optical bandgap calculated based on Tauc plot (inset) of $(S\text{-MBA})_4Bi_2Cl_{10}$.

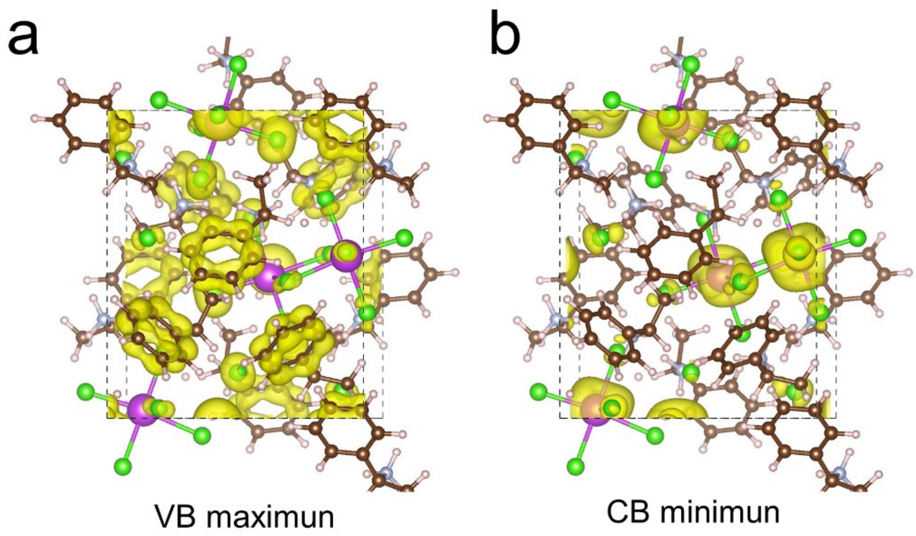

Fig. S7 Isosurface plots of the wave functions of (a) VB maximum and (b) CB minimum of (*S*-MBA)$_4$Bi$_2$Cl$_{10}$.

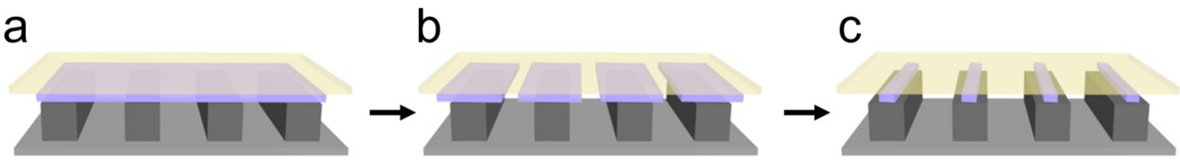

Fig. S8 Schematic diagram of capillary-bridge assembly system to fabricate the 0D lead-free perovskite microwire arrays with high crystallinity and pure crystallographic orientation. (a) Liquid thin film forming between the substrate and the micropillar template. (b) Discrete capillary bridges forming on the hydrophilic micropillar tops. (c) Perovskite microwire array with uniform morphology forming on the substrate after complete evaporation of the solvent.

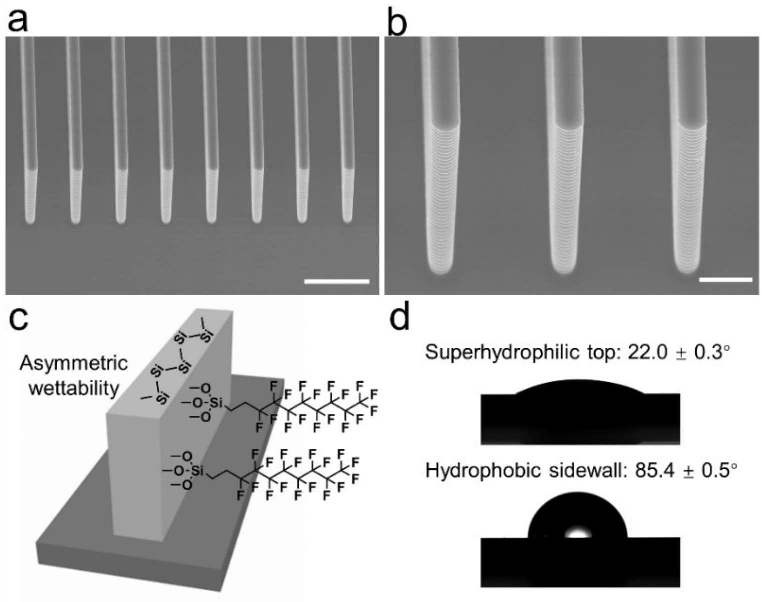

Fig. S9 (a) Large-scale and (b) zoom-in SEM images of micropillars with a width of 2 μm and adjacent distance of 5 μm. Scale bars: (a) 10 μm, (b) 3 μm. (c) Schematic illustration of the template showing the hydrophilic pillar top and hydrophobic sidewall selectively modified by heptadecafluorodecyltrimethoxysilane (FAS) molecules. (d) The contact angles of DMSO on the pillar top (22.0 ± 0.3°) and the sidewall (85.4 ± 0.5°). The average contact angles are calculated from five different templates and the error bars represent the standard deviation.

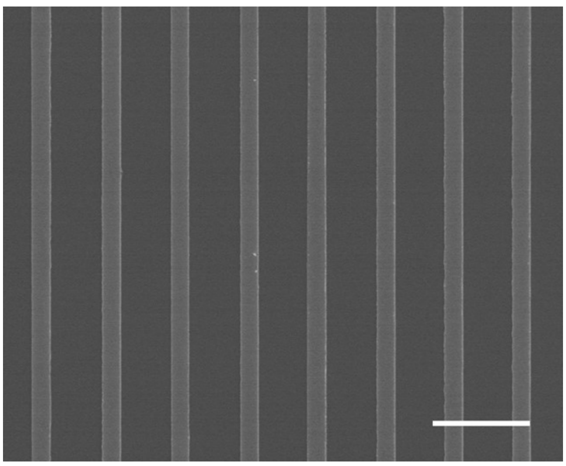

Fig. S10 SEM image of $(S\text{-MBA})_4Bi_2Cl_{10}$ microwire arrays showing precise location, strict isometric arrangement, and homogeneous size over a large area. Scale bar: 10 μm.

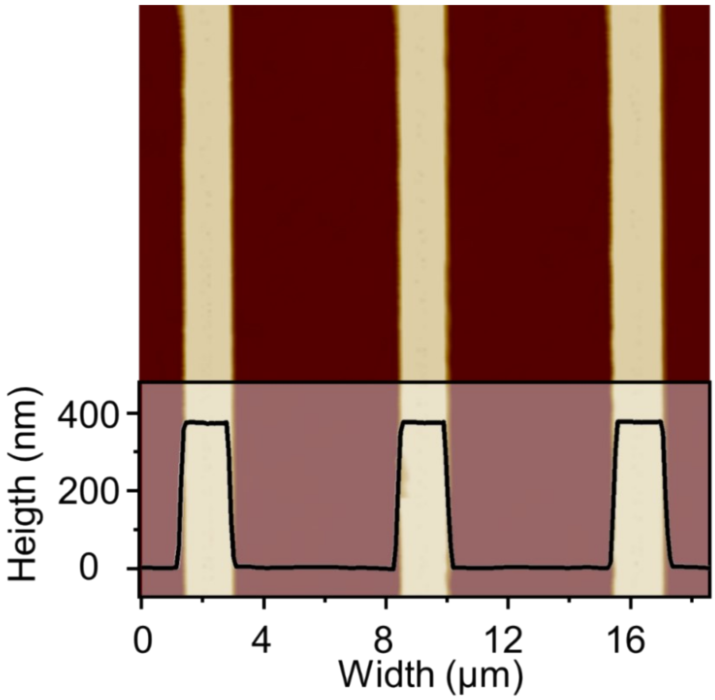

Fig. S11 AFM image of (S-MBA)$_4$Bi$_2$Cl$_{10}$ microwire arrays showing the smooth surface and uniform size with a height of about 370 nm, a width of about 1.9 μm, and the adjacent distance of about 5.1 μm.

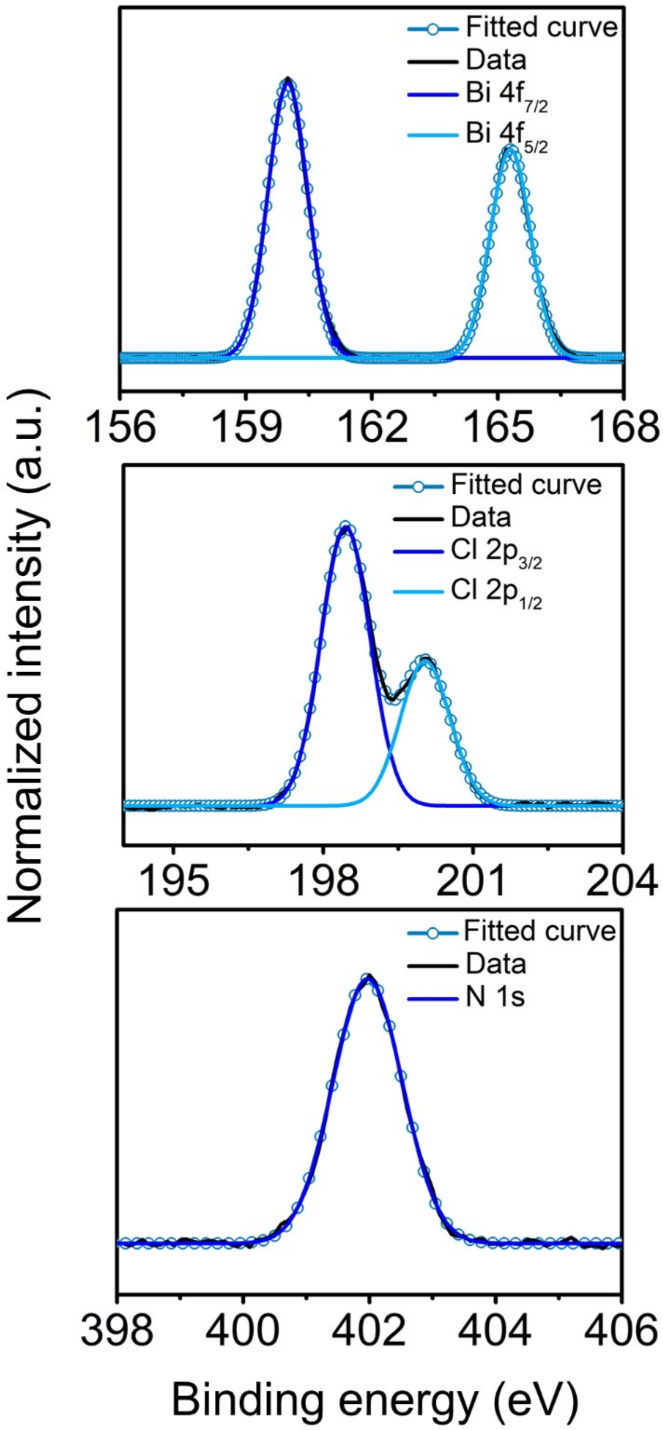

Fig. S12 XPS spectra of (S-MBA)$_4$Bi$_2$Cl$_{10}$ microwire arrays showing Bi 4f, Cl 2p, and N 1s regions.

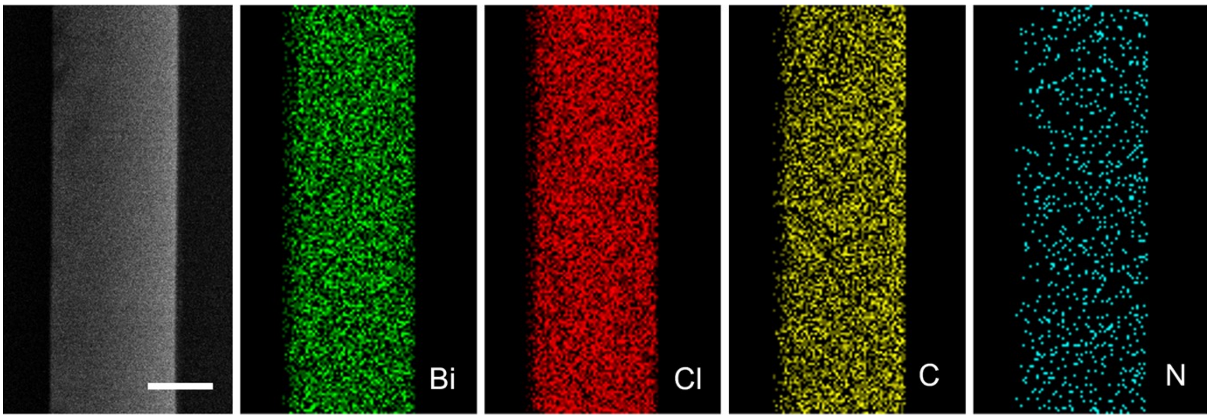

Fig. S13 Zoom-in SEM image and corresponding EDS element mappings of (R-MBA)$_4$Bi$_2$Cl$_{10}$ single microwire showing the uniform distribution of Bi, Cl, C, and N elements. Scale bar: 1 μm.

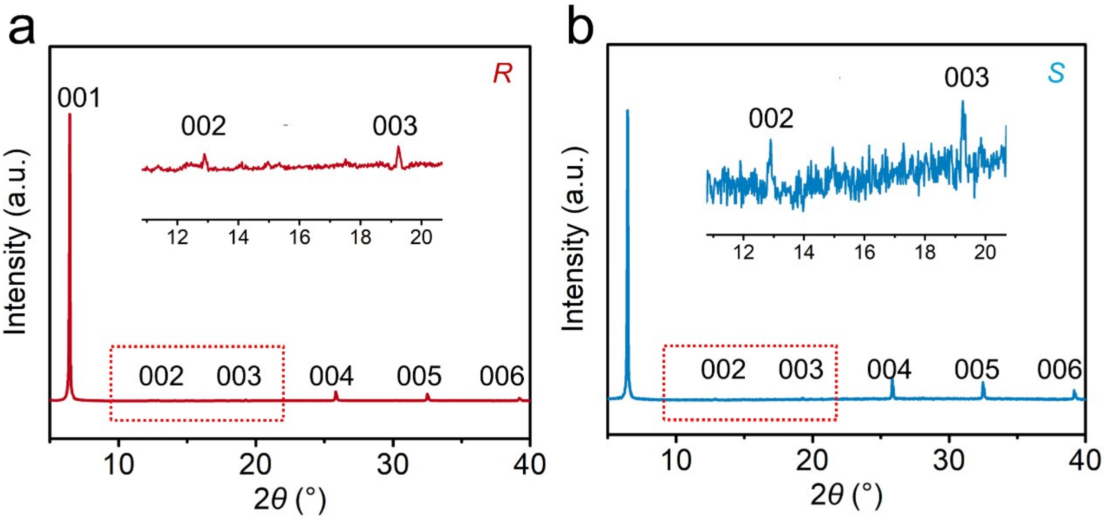

Fig. S14 XRD patterns of (a) (R-MBA)$_4$Bi$_2$Cl$_{10}$ and (b) (S-MBA)$_4$Bi$_2$Cl$_{10}$ microwire arrays. Insets are the details corresponding to (002) and (003) plane.

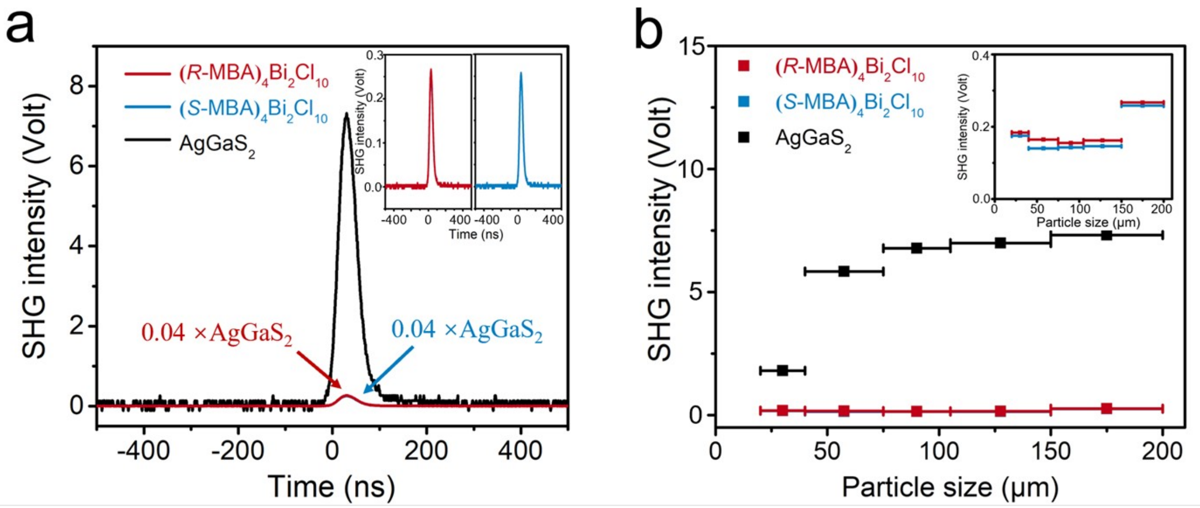

Fig. S15 (a) Measured SHG signals of (R-MBA)$_4$Bi$_2$Cl$_{10}$ sieved powder with 150−200 μm particle size and (b) particle-size-dependent SHG intensity of (R-MBA)$_4$Bi$_2$Cl$_{10}$ sieved powder with AgGaS$_2$ crystals as references. The pump wavelength is 2090 nm. The SHG intensity of (R/S-MBA)$_4$Bi$_2$Cl$_{10}$ powder is almost identical, resulting in the coincidence of (R/S-MBA)$_4$Bi$_2$Cl$_{10}$ curves in (a) and (b), which is indistinguishable.

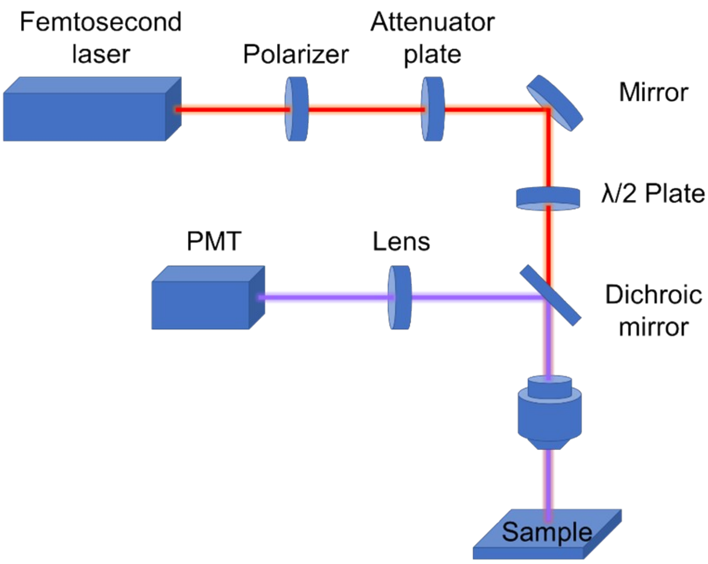

Fig. S16 The schematic illustration of the home-built femtosecond laser setup for SHG signal measurement of microwires.

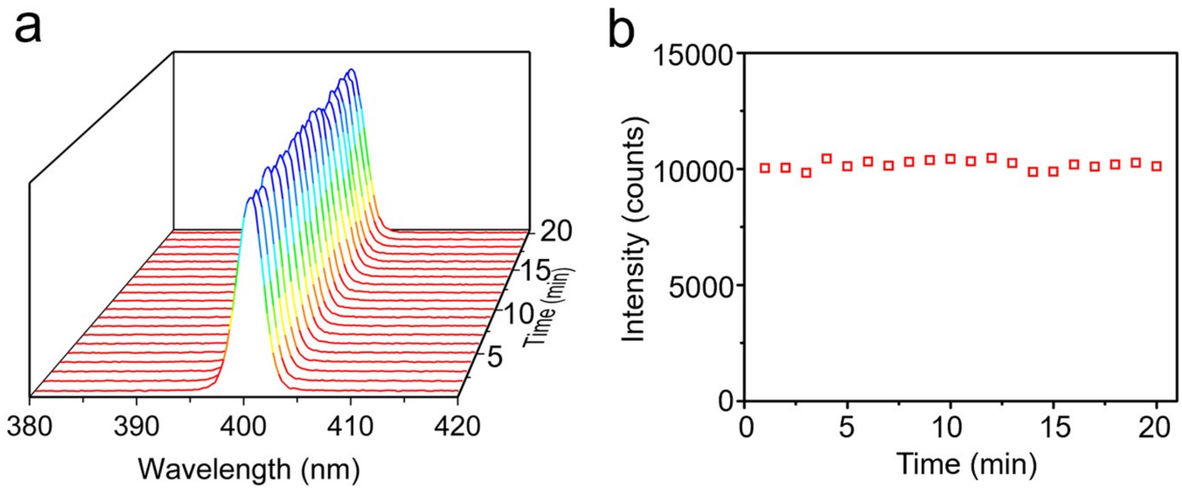

Fig. S17 Laser stability of perovskite microwire arrays. (a) SHG spectra of the (R-MBA)$_4$Bi$_2$Cl$_{10}$ microwire under continuous radiation with a pump wavelength of 800 nm. (b) SHG intensity for different times corresponding to (a).

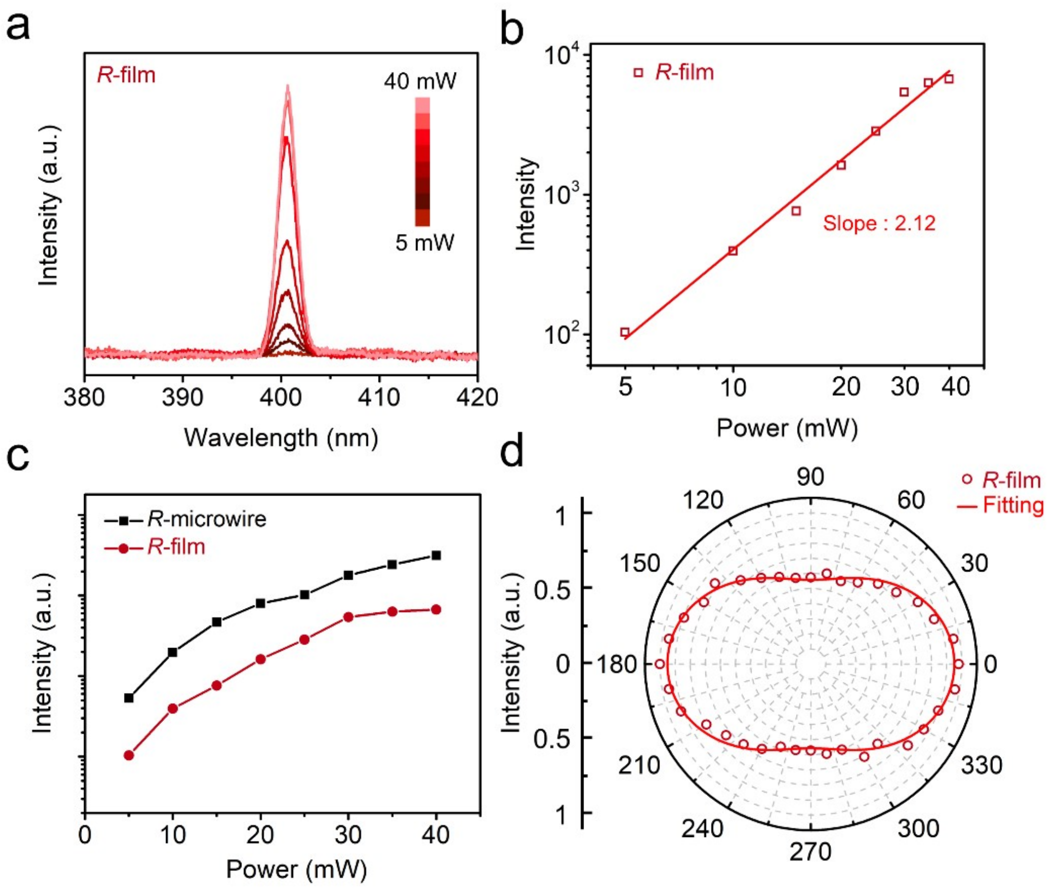

Fig. S18 (a) Power-dependent SHG intensity of (R-MBA)$_4$Bi$_2$Cl$_{10}$ polycrystalline film with a pump wavelength of 800 nm. (b) Logarithmic plot of SHG intensity as a function of the incident power corresponding to (a). (c) Comparison of SHG intensities of single-crystalline microwire array and polycrystalline film of (R-MBA)$_4$Bi$_2$Cl$_{10}$ under the same excitation conditions. (d) Normalized polarization-dependent SHG intensity of (R-MBA)$_4$Bi$_2$Cl$_{10}$ polycrystalline film showing a polarization ratio of 0.272, which is smaller than that of single-crystalline microwire arrays.

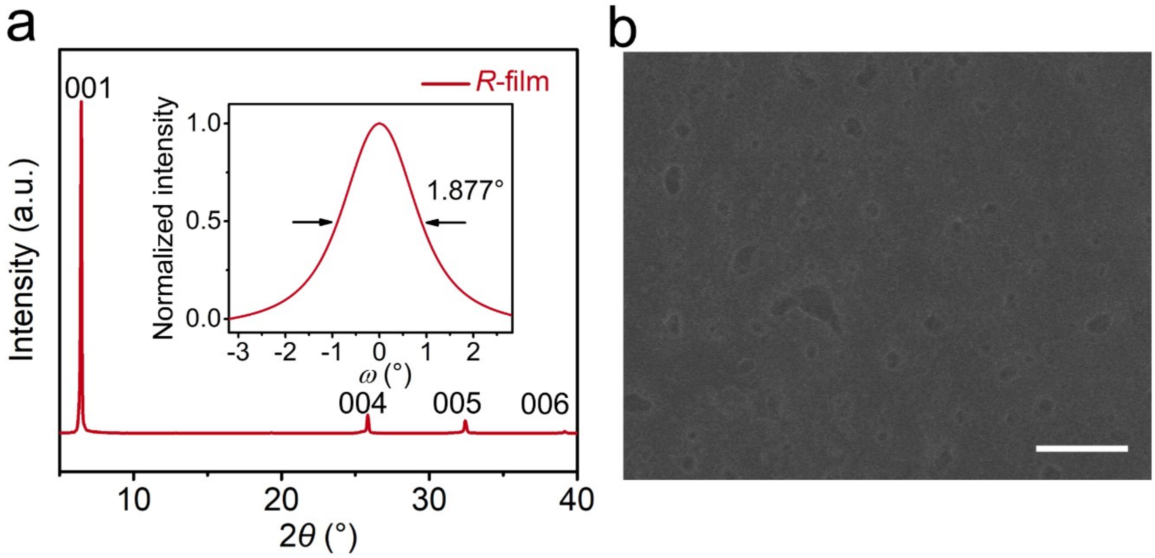

Fig. S19 (a) XRD pattern and rocking curve corresponding to (001) plane (inset) of (*R*-MBA)$_4$Bi$_2$Cl$_{10}$ polycrystalline film showing a broad peak with full width at half maximum of 1.877°, which is bigger than that of (*R*-MBA)$_4$Bi$_2$Cl$_{10}$ single-crystalline microwire array, indicating the poor crystallinity of the polycrystalline film. (b) SEM image of (*R*-MBA)$_4$Bi$_2$Cl$_{10}$ polycrystalline film showing a large number of grain boundaries. Scale bar: 3 μm.

Table S1. Crystallographic data of and structure refinement for (R-MBA)$_4$Bi$_2$Cl$_{10}$ and (S-MBA)$_4$Bi$_2$Cl$_{10}$.

Compound	**(R-MBA)$_4$Bi$_2$Cl$_{10}$**	**(S-MBA)$_4$Bi$_2$Cl$_{10}$**
Empirical formula	$Bi_2Cl_{10}\cdot 4(C_8H_{12}N)$	$Bi_2Cl_{10}\cdot 4(C_8H_{12}N)$
Formula weight	1261.20	1261.20
Temperature /K	170	170
Crystal system	Monoclinic	Monoclinic
Space group	$P2_1$	$P2_1$
a /Å	11.6344(3)	11.6866(2)
b /Å	14.3276(3)	14.3235(3)
c /Å	13.6062(3)	13.5914(3)
α /°	90	90
β /°	94.890(2)	94.833(2)
γ /°	90	90
Volume /Å^3	2259.80(9)	2267.02(8)
Z	2	2
ρ_{calc} /g cm^{-3}	1.854	1.848
μ /mm^{-1}	8.40	8.37
F(000)	1208	1208
Radiation	Mo Kα (λ = 0.71073 Å)	Mo Kα (λ = 0.71073 Å)
2θ range /°	4−59	3.6−59.6
Index ranges	$-16 \le h \le 15$	$-16 \le h \le 15$

	$-20 \le k \le 19$	$-19 \le k \le 20$
	$-18 \le l \le 19$	$-17 \le l \le 19$
Reflections collected	42947	43483
Independent reflections	12118 [R_{int} = 0.095]	12240 [R_{int} = 0.049]
Data/restraints/parameters	12118/61/440	12240/63/441
Goodness-of-fit on F^2	1.03	1.12
Final R indexes [I>=2σ (I)]	R_1 = 0.0524, wR_2 = 0.1295	R_1 = 0.0626, wR_2 = 0.1512
Final R indexes [all data]	R_1 = 0.0628, wR_2 = 0.1331	R_1 = 0.0752, wR_2 = 0.1566
Largest diff. peak/hole /e Å^{-3}	2.02/−2.10	2.94/−3.51
Flack parameter	0.006(7)	0.003(10)

Table S2. Selected bond lengths for (R-MBA)$_4$Bi$_2$Cl$_{10}$ and (S-MBA)$_4$Bi$_2$Cl$_{10}$.

(R-MBA)$_4$Bi$_2$Cl$_{10}$			**(S-MBA)$_4$Bi$_2$Cl$_{10}$**		
Atom	**Atom**	**Length /Å**	**Atom**	**Atom**	**Length /Å**
Bi1	Cl1	2.515(3)	Bi1	Cl1	2.562(4)
Bi1	Cl2	2.704(4)	Bi1	Cl2	2.513(4)
Bi1	Cl3	2.638(3)	Bi1	Cl3	2.701(4)
Bi1	Cl4	2.683(3)	Bi1	Cl4	2.711(4)
Bi1	Cl5	2.812(3)	Bi1	Cl5	2.880(3)
Bi1	Cl6	2.984(3)	Bi1	Cl6	3.011(4)
Bi2	Cl5	3.012(3)	Bi2	Cl5	2.982(3)
Bi2	Cl6	2.869(3)	Bi2	Cl6	2.813(3)
Bi2	Cl7	2.701(3)	Bi2	Cl7	2.701(4)
Bi2	Cl8	2.515(3)	Bi2	Cl8	2.516(4)
Bi2	Cl9	2.707(3)	Bi2	Cl9	2.648(4)
Bi2	Cl10	2.557(4)	Bi2	Cl10	2.686(4)

Table S3. Selected bond angles for (R-MBA)$_4$Bi$_2$Cl$_{10}$ and (S-MBA)$_4$Bi$_2$Cl$_{10}$.

(***R***-**MBA)$_4$Bi$_2$Cl$_{10}$**				(***S***-**MBA)$_4$Bi$_2$Cl$_{10}$**			
Atom	**Atom**	**Atom**	**Angle /°**	**Atom**	**Atom**	**Atom**	**Angle /°**
Cl1	Bi1	Cl2	96.53(14)	Cl1	Bi1	Cl3	88.69(14)
Cl1	Bi1	Cl3	91.97(13)	Cl1	Bi1	Cl4	90.97(15)
Cl1	Bi1	Cl4	90.29(14)	Cl1	Bi1	Cl5	177.27(14)
Cl1	Bi1	Cl5	91.14(11)	Cl1	Bi1	Cl6	96.62(13)
Cl1	Bi1	Cl6	174.43(12)	Cl2	Bi1	Cl1	93.38(14)
Cl2	Bi1	Cl5	88.20(13)	Cl2	Bi1	Cl3	90.73(13)
Cl2	Bi1	Cl6	85.85(12)	Cl2	Bi1	Cl4	95.08(13)
Cl3	Bi1	Cl2	91.23(14)	Cl2	Bi1	Cl5	87.40(12)
Cl3	Bi1	Cl4	89.08(11)	Cl2	Bi1	Cl6	169.98(11)
Cl3	Bi1	Cl5	176.89(10)	Cl3	Bi1	Cl4	174.19(12)
Cl3	Bi1	Cl6	93.01(10)	Cl3	Bi1	Cl5	88.69(12)
Cl4	Bi1	Cl2	173.16(10)	Cl3	Bi1	Cl6	88.80(12)
Cl4	Bi1	Cl5	91.14(11)	Cl4	Bi1	Cl5	91.57(14)
Cl4	Bi1	Cl6	87.31(11)	Cl4	Bi1	Cl6	85.47(12)

Cl5	Bi1	Cl6	83.90(9)	Cl5	Bi1	Cl6	82.59(9)
Cl6	Bi2	Cl5	82.42(8)	Cl6	Bi2	Cl5	84.22(10)
Cl7	Bi2	Cl5	88.70(11)	Cl7	Bi2	Cl5	85.74(13)
Cl7	Bi2	Cl6	88.84(11)	Cl7	Bi2	Cl6	88.24(15)
Cl7	Bi2	Cl9	174.33(11)	Cl8	Bi2	Cl5	175.00(13)
Cl8	Bi2	Cl5	169.78(11)	Cl8	Bi2	Cl6	91.58(13)
Cl8	Bi2	Cl6	87.37(11)	Cl8	Bi2	Cl7	96.87(16)
Cl8	Bi2	Cl7	90.60(12)	Cl8	Bi2	Cl9	91.81(14)
Cl8	Bi2	Cl9	95.06(12)	Cl8	Bi2	Cl10	90.02(15)
Cl8	Bi2	Cl10	93.20(14)	Cl9	Bi2	Cl5	92.39(11)
Cl9	Bi2	Cl5	85.78(10)	Cl9	Bi2	Cl6	176.60(12)
Cl9	Bi2	Cl6	91.70(12)	Cl9	Bi2	Cl7	91.49(15)
Cl10	Bi2	Cl5	96.98(12)	Cl9	Bi2	Cl10	89.21(12)
Cl10	Bi2	Cl6	177.32(13)	Cl10	Bi2	Cl5	87.33(12)
Cl10	Bi2	Cl7	88.54(13)	Cl10	Bi2	Cl6	90.65(12)
Cl10	Bi2	Cl9	90.86(14)	Cl10	Bi2	Cl7	173.05(11)
Bi1	Cl5	Bi2	97.06(8)	Bi1	Cl5	Bi2	96.12(9)

Bi2	Cl6	Bi1	96.48(8)	Bi2	Cl6	Bi1	96.92(10)

Table S4. Comparison of second-order NLO properties of perovskites.

Materials	Dimension	Transparency[a] [nm]	Morphology	Exciting wavelength [nm]	NLO coefficient[b] d_{eff} [pm V^{-1}]	Anisotropy ratio[c]	Ref.
Low dimensional lead-free perovskites							
(R/S-MBA)$_4$Bi$_2$Cl$_{10}$	0D	364-3191	Microwire	800	2.72	0.992	This work
(R-C$_8$H$_{12}$N)$_4$Bi$_2$Br$_{10}$	0D	-	Powder	1064	20 × α-SiO$_2$	-	[1]
(C$_8$H$_{11}$NF)$_4$Bi$_2$Br$_{10}$	0D	-	Crystal plate	800	1/45 × α-SiO$_2$	-	[2]
(R-1-1NEA)$_2$CuCl$_4$	0D	-	Film	880	0.13	0.84	[3]
(R/S-MBA)$_2$CuCl$_4$	2D	-	Crystal plate	800	0.35	-	[4]
(R/S-3AP)$_4$AgBiBr$_{12}$	2D	-	Microwire	800	0.28	0.9/0.92	[5]
(CPA)$_4$AgBiBr$_8$	2D	-	Powder	1064	0.55 × KDP	-	[6]
Low dimensional lead perovskites							
(R/S-2-C$_5$H$_{14}$N$_2$)$_2$PbI$_6$	0D	~2000-3000	Single crystal	960	2 × Y-cut quartz	-	[7]
C$_5$H$_{14}$N$_2$PbCl$_4$·H$_2$O	1D	-	mm-sized samples	1064	0.83 × KDP	-	[8]
(R/S-3-aminopiperidine)PbI$_4$	1D	~700-1100	bulk crystal	1064	2.1 × KDP	0.83	[9]
PEA$_3$PbBr$_5$·H$_2$O	1D	-	Single crystal	900	0.1	0.94	[10]
(PMA)$_2$PbCl$_4$	2D	-	Single crystal	1550	1.4	-	[11]

$(2\text{-FBA})_2PbCl_4$	2D	-	Single crystal	1064	0.35	-	[12]
$(R\text{-MPEA})_{1.5}PbBr_{3.5}(DMSO)_{0.5}$	2D	-	Nanowire	850	0.68	0.96	[13]
$(BA)_2(EA)_2Pb_3I_{10}$	2D	-	Powder	1064	0.4 × KDP	-	[14]

[a]Transparency window reflects the range of bands in which the crystal can be applied; the wider the window, the wider the wavelength range in which frequency conversion can be achieved. [b]NLO coefficient reflects the frequency conversion efficiency of a crystal; the larger the nonlinearity coefficient, the higher the conversion efficiency of frequency doubling. [c]Anisotropy ratio reflects the material's sensitivity to linearly polarized fundamental frequency light; the closer the value is to 1, the more pronounced the anisotropy of the crystal is. d_{eff} (KDP) = 0.39 pm V^{-1}; d_{eff} (Y-cut quartz) = 0.3 pm V^{-1}.

The results show that $(R/S\text{-MBA})_4Bi_2Cl_{10}$ in our work exhibit higher NLO coefficient and anisotropy ratio, and are transparent over a broad spectral range, showing excellent NLO performances, which might provide a strategy for NLO-integrated applications in advancing photonics devices.

[1] T. H. Moon, S. J. Oh and K. M. Ok, $[((R)\text{-}C_8H_{12}N)_4][Bi_2Br_{10}]$ and $[((S)\text{-}C_8H_{12}N)_4][Bi_2Br_{10}]$: chiral hybrid bismuth bromides templated by chiral organic cations, *ACS Omega*, 2018, **3**, 17895−17903.

[2] N. Dehnhardt, M. Axt, J. Zimmermann, M. Yang, G. Mette and J. Heine, Band gap-tunable, chiral hybrid metal halides displaying second-harmonic generation, *Chem. Mater.*, 2020, **32**, 4801−4807.

[3] Z. H. Guo, J. Z. Li, J. C. Liang, C. S. Wang, X. Zhu and T. C. He, Regulating optical activity and anisotropic second-harmonic generation in zero-dimensional hybrid copper

halides, *Nano Lett.*, 2022, **22**, 846−852.

[4] Z. Guo, J. Li, C. Wang, R. Liu, J. Liang, Y. Gao, J. Cheng, W. Zhang, X. Zhu, R. Pan and T. He, Giant optical activity and second harmonic generation in 2D hybrid copper halides, *Angew. Chem. Int. Ed.*, 2021, **60**, 8441−8445.

[5] Z. W. Yu, S. Q. Cao, Y. J. Zhao, Y. W. Guo, M. Q. Dong, Y. Fu, J. J. Zhao, J. R. Yang, L. Jiang and Y. C. Wu, Chiral lead-free double perovskite single-crystalline microwire arrays for anisotropic second-harmonic generation, *ACS Appl. Mater. Interfaces*, 2022, **14**, 39451−39458.

[6] W. Q. Guo, X. T. Liu, S. G. Han, Y. Liu, Z. Y. Xu, M. C. Hong, J. H. Luo and Z. H. Sun, Room-temperature ferroelectric material composed of a two-dimensional metal halide double perovskite for X-ray detection, *Angew. Chem. Int. Ed.*, 2020, **10**, 13983−13988.

[7] X. D. Jia, Y. S. Zheng, P. X. Cheng, X. Han, L. Xu and J. L. Xu, Methylpiperazine based 0D chiral hybrid lead halides for second harmonic generation, *Dalton Trans.*, 2022, **51**, 7248−7254.

[8] Y. Peng, Y. P. Yao, L. N. Li, Z. Y. Wu, S. S. Wang and J. H. Luo, White-light emission in a chiral one-dimensional organic–inorganic hybrid perovskite, *J. Mater. Chem. C*, 2018, **6**, 6033−6037.

[9] D. Y. Fu, J. L. Xin, Y. Y. He, S. C. Wu, X. Y. Zhang, X. M. Zhang and J. H. Luo, Chirality-dependent second-order nonlinear optical effect in 1D organic–inorganic hybrid perovskite bulk single crystal, *Angew. Chem. Int. Ed.*, 2021, **60**, 20021−20026.

[10] Y. K. Zhou, W. Li, X. Chen, X. Z. Li, X. J. Wang, B. Bai, Y. Chen and H. H. Fang, Efficient second-order nonlinear response and upconversion emission from a wide-

bandgap quasi-1D lead bromide perovskite, *J. Mater. Chem. C*, 2022, **10**, 15424−15430.

[11] Y. Gao, G. Walters, Y. Qin, B. Chen, Y. Min, A. Seifitokaldani, B. Sun, P. Todorovic, M. I. Saidaminov, A. Lough, S. Tongay, S. Hoogland and E. H. Sargent, Electro-optic modulation in hybrid metal halide perovskites, *Adv. Mater.*, 2019, **31**, e1808336.

[12] P. P. Shi, S. Q. Lu, X. J. Song, X. G. Chen, W. Q. Liao, P. F. Li, Y. Y. Tang and R. G. Xiong, Two-dimensional organic-inorganic perovskite ferroelectric semiconductors with fluorinated aromatic spacers, *J. Am. Chem. Soc.*, 2019, **141**, 18334−18340.

[13] C. Q. Yuan, X. Y. Li, S. Semin, Y. Q. Feng, T. Rasing and J. L. Xu, Chiral lead halide perovskite nanowires for second-order nonlinear optics, *Nano Lett.*, 2018, **18**, 5411−5417.

[14] S. G. Han, X. T. Liu, Y. Liu, Z. Y. Xu, Y. B. Li, M. C. Hong, J. H. Luo and Z. H. Sun, High-temperature antiferroelectric of lead iodide hybrid perovskites, *J. Am. Chem. Soc.*, 2019, **141**, 12470−12474.